Journal of Materials Chemistry B

ROYAL SOCIETY OF CHEMISTRY

PAPER

View Article Online
View Journal | View Issue

Check for updates

Cite this: J. Mater. Chem. B, 2024, 12, 5111

Published on 18 kwietnia 2024. Downloaded on 21.04.2026 23:01:02.

Copper peroxide nanodot-decorated gold nanostar/silica nanorod Janus nanostructure with NIR-II photothermal and acid-triggered hydroxyl radical generation properties for the effective treatment of wound infections†

Yan Lu,‡ Rui Xu,‡ Wei Liu,‡ Xiling Song, Wanqin Cai, Yuan Fang, Wei Xue* and Siming Yu *

Received 13th March 2024,
Accepted 18th April 2024

DOI: 10.1039/d4tb00536h

rsc.li/materials-b

Recently, bacterial infections have become a global crisis, greatly threatening the health of human beings. The development of a non-antibiotic biomaterial is recognized as an alternative way for the effective treatment of bacterial infections. In the present work, a multifunctional copper peroxide (CP) nanodot-decorated gold nanostar (GNS)/silica nanorod (SiNR) Janus nanostructure (GNS@CP/SiNR) with excellent antibacterial activity was reported. Due to the formation of the Janus nanostructure, GNS@CP/SiNR displayed strong plasmonic resonance absorbance in the near infrared (NIR)-II region that enabled the nanosystem to achieve mild photothermal therapy (MPTT). In acidic conditions, CP decorated on GNS@CP/SiNR dissociated rapidly by releasing Cu^{2+} and H_2O_2, which subsequently transformed to •OH *via* the Fenton-like reaction for chemodynamic therapy (CDT). As a result, GNS@CP/SiNR could effectively inhibit both Gram-negative *Escherichia coli* (*E. coli*) and Gram-positive *Staphylococcus aureus* (*S. aureus*), and eradicate the associated bacterial biofilms by exerting the synergistic MPTT/CDT antibacterial effect. Moreover, GNS@CP/SiNR was also demonstrated to be effective in treating wound infections, as verified on the *S. aureus*-infected full thickness excision wound rat model. Our mechanism study revealed that the synergistic MPTT/CDT effect of GNS@CP/SiNR firstly caused bacterial membrane damage, followed by boosting intracellular ROS *via* the severe oxidative stress effect, which subsequently caused the depletion of intracellular GSH and DNA damage, finally leading to the death of bacteria.

1. Introduction

In recent years, global public health is being greatly threatened by bacterial infections. In 2019, the global infection-related death number was reported to be approximately 13.7 million, which ranked as the second leading cause of death globally.[1] Antibiotics are the most common way for treating bacterial infections, but its overuse has already lead to the development of bacterial resistance, which in turn has caused the failure of many antibiotics. It is estimated that approximately 3 million patients suffer from resistant bacterial infections, which has caused at least 35 000 deaths each year.[2] Nowadays, the development rate of novel antibiotics has fallen seriously behind the appearances of new bacterial resistance, leaving vancomycin as the last resort. However, the rise of vancomycin-resistant *Staphylococcus aureus* (VRSA) and *Enterococci* (VRE) urged scientists to develop novel antibacterial materials to combat the resistant bacterial infection crisis.[3,4]

Recently, nanomaterial-based photothermal therapy (PTT) has attracted enormous interest in antibacterial applications, mainly due to its easy operation, high antibacterial efficiency and slim chance of inducing bacterial resistance.[5,6] The photothermal effect-induced heat elevation can effectively kill bacteria by ways of breaking the bacterial membrane, denaturing the enzyme activity, causing severe oxidative stress, damaging bacterial DNA, *etc.*[7] Currently, many types of nanomaterial-based photothermal reagents have been developed for photothermal therapy, including organic dye (*i.e.*, indocyanine green, polypyrrole, melanin)-based assemblies,[8] gold (Au) nanostructures,[9–11] carbon-based materials, molybdenum-based materials,[12] and two-dimensional materials (graphene, MXenes, black phosphorus nanosheets, *etc.*).[13] However, the photothermal property

Key Laboratory of Biomaterials of Guangdong Higher Education Institutes, Department of Biomedical Engineering, Jinan University, Guangzhou 510632, China. E-mail: siming_yu@hotmail.com, weixue_jnu@hotmail.com

† Electronic supplementary information (ESI) available. See DOI: https://doi.org/10.1039/d4tb00536h

‡ Authors contributed equally to this work.

Published on 18 kwietnia 2024. Downloaded on 21.04.2026 23:01:02.

of the current materials is mainly located in the near infrared I window (NIR-I, 650–950 nm), which can also cause damage to the normal tissues because the tissues themselves can absorb NIR-I light and transform it into heat.[14] Instead, photothermal materials in the NIR-II window (1000–1200 nm) display higher biocompatibility because the NIR-II range is almost transparent to tissues.[15–18] In addition, because a strong photothermal effect can also burn the normal tissues and result in many side effects, mild-photothermal therapy (MPTT) has been developed and was demonstrated to be the safer therapeutic methodology.[19] Nevertheless, it is difficult for MPTT alone to completely inhibit the bacterial growth; its combination with other therapeutic strategies is necessary in order to achieve satisfying antibacterial outcomes.[19–21] Therefore, developing NIR-II photothermal materials with synergistic MPTT antibacterial properties is of high demand.

Chemodynamic therapy (CDT) is a recently emerging therapeutic methodology that is being widely explored for many biomedical applications, such as cancer therapy, antibacterial application, *etc.*[22] In a typical CDT, the Fenton material (*e.g.*, Fe_3O_4) can firstly release Fe^{2+} in an acid environment, and subsequently react with H_2O_2 to produce highly toxic hydroxyl radical ($^{\bullet}OH$) *via* the classic Fenton reaction.[23] The generated $^{\bullet}OH$ can induce severe oxidative stress to bacteria, and finally lead to bacterial death by ways of lipid peroxidation, protein inactivation and DNA damage.[24] Although CDT can effectively inhibit bacterial growth *in vitro*, the antibacterial efficiency of CDT is largely restricted in *in vivo* applications because of the limited H_2O_2 supply level in the bacterial infection microenvironment (IME). To resolve the drawbacks, many strategies have been established in order to increase the H_2O_2 supply level in IME, such as co-delivery of glucose oxidase (GOx),[25] utilizing external physical stimuli (*e.g.*, alternating magnetic field, red light),[26,27] or using metal peroxide (CaO_2, CuO_2, MgO_2, *etc.*).[28] Among those, copper peroxide (CuO_2) is considered as an ideal H_2O_2-producing material because it can rapidly dissociate in a weak acidic environment by simultaneously releasing Cu^{2+} and H_2O_2. In addition, CuO_2 can effectively produce $^{\bullet}OH$ *via* the Fenton-like reaction between the released Cu^{2+} and H_2O_2.[29] However, it remains a big challenge for CDT-based materials to cross the bacterial membrane and the associated biofilms to exert the designed antibacterial effect.[30] Since previous studies have indicated that MPTT is capable of breaking the bacterial membrane and eradicating the bacterial biofilm, a combination of MPTT and CDT is supposed to be an ideal way to achieve highly-efficient antibacterial applications.

In the present work, a multifunctional copper peroxide (CP) nanodots decorated gold nanostar (GNS)/silica nanorod (SiNR) Janus nanostructure (GNS@CP/SiNR) was rationally designed and fabricated by integrating the NIR-II MPTT and CDT properties. Due to the formation of the Janus nanostructure, GNS@CP/SiNR displayed strong plasmonic resonance absorbance in the NIR-II region, which endowed the nanosystem with a mild-photothermal effect upon 1064 nm laser irradiation. Under acidic conditions, CP decorated on GNS@CP/SiNR dissociated rapidly by releasing Cu^{2+} and H_2O_2, and subsequently transformed to $^{\bullet}OH$ *via* the Fenton-like reaction. Upon encountering bacteria, the positive GNS@CP/SiNR could effectively anchor to the negative bacterial membrane through electrostatic interactions. Upon NIR-II 1064 nm laser irradiation, GNS@CP/SiNR exerted a synergistic MPTT/CDT antibacterial effect by effectively inhibiting both Gram-negative *Escherichia coli* (*E. coli*) and Gram-positive *Staphylococcus aureus* (*S. aureus*), as well as eradicating the associated bacterial biofilms. The excellent MPTT/CDT antibacterial effect of GNS@CP/SiNR was also verified on the *S. aureus*-infected full thickness excision wound rat model. Our mechanism study revealed that the synergistic MPTT/CDT effect firstly damaged the bacterial membrane by accelerating the release of intracellular protein components and enhancing the penetration of GNS@CP/SiNR. As followed, the intracellular ROS generation was boosted *via* the severe oxidative stress effect, which subsequently caused the depletion of intracellular GSH and DNA damage, finally leading to bacterial death. The findings of our work provide a promising material for the highly-efficient treatment of wound infections.

Siming Yu

Dr Siming Yu obtained his PhD degree in Materials Science from Universitat Autònoma de Barcelona (Institute of Materials Science of Barcelona, ICMBA-CSIC, Spain) in 2015. After graduation, he joined the Biomedical Engineering Department of Jinan University as a lecturer. In the year of 2020, he was promoted as an associate professor. His research focuses on the rational design of smart biomedical materials for anticancer and antibacterial applications. Currently, he has published 32 peer-reviewed papers in Advanced Functional Materials, Chemistry of Materials, Chemical Engineering Journal, Journal of Materials Chemistry B, and others.

2. Experimental sections

2.1 Materials

Chloroauric acid ($HAuCl_4 \cdot 3H_2O$) was purchased from Shanghai Aladdin Reagent Company, and tetraethyl orthosilicate (TEOS, 98%) was purchased from Shanghai Macklin Reagent Company. Copper(II) chloride dihydrate ($CuCl_2 \cdot 2H_2O$), silver nitrate ($AgNO_3$), polyvinylpyrrolidone (PVP, average Mw 10 000), potassium permanganate ($KMnO_4$, $\geq$99.5%), cetyltrimethylammonium bromide (CTAB), L-ascorbic acid (AA), and 3-mercaptopropyltrimethoxysilane (MPTMS) were purchased from Sigma-Aldrich (MO, USA). Sodium hydroxide (NaOH), hydrochloric acid (HCl, 37%), hydrogen peroxide (H_2O_2, 30%), ammonium hydroxide ($NH_3 \cdot H_2O$, 28%) and bovine serum albumin (BSA) were purchased from Aladdin (Shanghai, China). Anhydrous ethanol was purchased from Damao Chemical Reagent Factory (Tianjin, China).

This journal is © The Royal Society of Chemistry 2024

Published on 18 kwietnia 2024. Downloaded on 21.04.2026 23:01:02.

Strains of *Escherichia coli* (*E. coli* ATCC 25922) and *Staphylococcus aureus* (*S. aureus* ATCC 29213) were purchased from Guangdong Microbial Culture Collection Center (Guangzhou, China). Lysogeny broth (LB) and LB agar were purchased from Coolaber Technology Co., Ltd (Beijing, China). The terminal-deoxynucleotidyl transferase-mediated nick end labeling (TUNEL) assay kit and 2′,7′-dichlorodihydrofluorescein diacetate (DCFH-DA) were obtained from Keygen Biotechnology Co., Ltd (Jiangsu, China). The live/dead Baclight bacterial viability assay kit (L7012), fetal bovine serum (FBS), and Dulbecco's modified eagle's medium (DMEM) were bought from Thermo Fisher Scientific, Inc. (MA, USA). ThiolTrace Violet 500 was purchased from AAT Bioquest (Sunnyvale, CA, USA). Hoechst 33342, cell counting kit-8 (CCK-8) was purchased from Dojindo Laboratories (Kumamoto, Japan).

2.2 Synthesis of the GNS@CP/SiNR Janus nanostructure

2.2.1 Synthesis of the mesoporous rod-like SiO_2 nanoparticles (SiNR). Firstly, cetyltrimethylammonium bromide (CTAB, 0.05 g) was dissolved in 10 mL ultrapure water under sonication condition, followed by slowly adding 1.29 mL $NH_3 \cdot H_2O$ under stirring. Then, the mixture was transferred to a glass vial, and 0.32 mL TEOS was slowly added and placed in an 80 °C oil bath to heat for 5 h. During the reaction process, the solution gradually changed from transparent to milky white. After that, the excess surfactant was removed by extraction with an ethanol/hydrochloric acid (HCl) mixture ($V_{Ethanol:HCl} = 10:1$) for 15 min. The precipitates were collected by centrifugation (10 000 rpm, 25 min) and washed three times with ethanol. Finally, the SiNR nanoparticles were re-suspended in 5 mL ultrapure water for further use.

2.2.2 Surface sulfhydrylation of SiNR (SiNR-SH). In detail, a 2-mL volume of SiNR suspension was dispersed in 10 mL of anhydrous ethanol, followed by adding 100 μL NaOH solution (0.1 M). After 10 min sonication, 200 μL PTMS was added. The reaction mixture was refluxed at 80 °C and stirred for 12 h. After that, the precipitates were collected by centrifugation (10 000 rpm, 25 min) and washed three times with anhydrous ethanol. Finally, sulfhydrylated SiNR (SiNR-SH) was obtained and resuspended in 3 mL ultrapure water for further use.

2.2.3 Synthesis of the Au-SiNR nanocomposite. Firstly, gold nanoparticles (Au NPs) were synthesized using the traditional citrate reduction method. Then, 10 mL Au NPs dispersion was placed in a 20 mL glass vial, 1.5 mL SiNR-SH was slowly added under magnetic stirring condition, followed by addition of 0.2 mL 0.2 M NaCl solution. The mixture was stirred at room temperature in the dark for 3 h. After the reaction, the precipitates were collected by centrifugation (1000 rpm, 10 min) and washed twice with ultrapure water. Finally, the Au-SiNR nanocomposite was obtained and re-suspended in 2 mL ultrapure water for further use.

2.2.4 Synthesis of the GNS/SiNR Janus nanostructure. Firstly, 10 μL 1.0 M HCl, 200 μL SiNR-SH, 75 μL 3 mM $AgNO_3$ solution, and 50 μL 0.1 M AA solution was added sequentially to 10 mL 0.25 mM $HAuCl_4$ solution. The mixture was stirred in the dark for 1 h reaction. After that, the precipitates were collected by centrifugation and washed twice with ultrapure water (3000 rpm, 10 min). Finally, the GNS/SiNR Janus nanostructure was re-suspended in 1 mL ultrapure water and set aside.

2.2.5 Synthesis of the GNS@CP/SiNR Janus nanostructure. Briefly, 0.3 g PVP and 0.5 g mL^{-1} GNS/SiNR suspensions were added sequentially to 1 mL $CuCl_2 \cdot 2H_2O$ (8.5 mg mL^{-1}). After stirring for 20 min, 1 mL 0.1 M NaOH solution and 100 μL 30% H_2O_2 solution were added sequentially. The reaction mixture was stirred for 30 min, and then transferred to a centrifuge tube. The precipitates were collected by centrifugation (3500 rpm, 15 min), and washed twice with ultrapure water. Finally, the GNS@CP/SiNR Janus nanostructure was obtained and re-suspended in 0.5 mL of water for further use.

2.3 Characterization

The morphology and size of GNS@CP/SiNR were characterized by transmission electron microscopy (TEM) (JEOL TEM-1210) at an operating voltage of 120 kV. Elemental mapping measurement was performed on a JEOL-2100 microscope with a voltage of 200 kV. UV-Vis spectra were recorded on a UV-2450/2250 (Shimadzu) spectrophotometer with a wavelength range from 190 to 2500 nm. The hydrodynamic diameter and the zeta potential measurements were conducted on a Zetasizer Nano ZS apparatus (Malvern). The X-ray photoelectron spectroscopy (XPS) measurements were performed on Thermo Scientific K-Alpha+ (Thermo Fisher, USA). X-ray diffraction (XRD) was performed on the X-ray powder diffractometer (XRD, XRX-7000×), where a freeze-dried sample powder was used.

2.4 Photothermal efficiency evaluation

The photothermal effects of GNS/SiNR and GNS@CP/SiNR were measured using an NIR thermal camera (220 s, Fotric). A 100-μL sample was added to an Eppendorf (EP) tube, and then irradiated with a NIR-II 1064 nm laser for 5 min. The temperature was recorded every 30 seconds, where PBS solution was used as the control. The photothermal performance of GNS@CP/SiNR was evaluated by irradiating with 1064 nm laser at different power densities of 0.5 W cm^{-2}, 1 W cm^{-2}, and 1.5 W cm^{-2}. The photothermal performance of materials with varied concentrations of 0 μg mL^{-1}, 75 μg mL^{-1}, 150 μg mL^{-1} and 300 μg mL^{-1} was also evaluated.

For the photothermal stability evaluation, the GNS@CP/SiNR dispersion (320 μg mL^{-1}) was irradiated by the 1064 nm laser (1 W cm^{-2}) for 5 min. Then, the laser was shut off to cool the sample to room temperature. During a 30 s interval, the temperature in the heating and cooling processes was recorded. The heating and cooling process was repeated five times, and the time–temperature curves were plotted to determine the photothermal stability of the nanosystem.

2.5 The acid-triggered Cu^{2+} release profile of GNS@CP/SiNR

Briefly, a 1-mL sample was dispersed in 9 mL PBS buffer solution of different pH values (5.5, 6.4, or 7.4), and gently shaken at 100 rpm. At different time intervals, the appropriate volume of samples was taken out, centrifuged and the supernatant was collected, then the Cu^{2+} concentration in the supernatant was

Published on 18 kwietnia 2024. Downloaded on 21.04.2026 23:01:02.

determined using the inductively coupled plasma emission spectrometer (ICP-OES, 5100 SVDV, Agilent, USA).

2.6 The acid-triggered H_2O_2 generation property of GNS@CP/SiNR

The H_2O_2 generation was detected using the potassium permanganate ($KMnO_4$)-based colorimetric assay. Briefly, 50 μL GNS@CP/SiNR (1 mg mL^{-1}) was added to 1 mL acidic $KMnO_4$ solution with the final material concentration of 50 μg mL^{-1}. After 10 min incubation, the color of the mixture was recorded using a digital camera and the UV-Vis spectra were measured using the UV-2450/2250 (Shimadzu) spectrophotometer with a wavelength range from 190 nm to 2500 nm. Additions of 10 μL H_2O_2 (1 M, resulting in a final H_2O_2 concentration of 10 mM) and 20 μL H_2O_2 (1 M, resulting in a final H_2O_2 concentration of 20 mM) were used as the positive control, and 1 mL $KMnO_4$ solution was used as the negative control.

To study the acidic pH-responsive H_2O_2 profiles of GNS@CP/SiNR, a 1-mL sample was dispersed in 9 mL PBS buffer solution with different pH values (5.5, 6.4 or 7.4), and gently shaken at 100 rpm. At different time intervals, the appropriate volume of samples was taken out, centrifuged and the supernatant was collected. The H_2O_2 concentration was determined using the same procedure as described above.

2.7 The acid-triggered hydrogen radical ($^{\bullet}OH$) generation property of GNS@CP/SiNR

The acid-triggered $^{\bullet}OH$ generation ability of GNS@CP/SiNR was detected using the 3,3′,5,5′-tetramethylbenzidine (TMB) assay. Briefly, 100 μL GNS@CP/SiNR was firstly added to 850 μL PBS buffer solution at pH 5.5, 6.4 and 7.4. Then, 50 μL TMB (10 mM) was added and incubated for 30 min. Finally, the color of the mixture was recorded using a digital camera and the UV-Vis spectra at wavelengths of 550–750 nm were measured using the UV-2450/2250 (Shimadzu) spectrophotometer with a wavelength range from 190 nm to 2500 nm.

The electron spin resonance was also used for $^{\bullet}OH$ detection using electron paramagnetic resonance spectroscopy (Magnettech ESR5000). Briefly, a 1-mL sample was dispersed in the PBS buffer solution at pH 5.5. After treatment with or without laser irradiation, the 5,5-dimethyl-1-pyrroline-*N*-oxide (DMPO) adduct was added and the samples were detected by ESR spectroscopy.

2.8 Bacterial culture

E. coli and *S. aureus* were grown in LB medium for 12 h in a 37 °C shaker. When the OD_{600} value of the bacterial culture reached 1.0, this suggested that the bacterial growth was in the logarithmic phase. The bacterial suspensions were then centrifuged and washed with 0.01 M PBS (pH 7.4) twice to remove the bacterial culture media. Finally, the bacterial pellets were redispersed in PBS to achieve a concentration of 1×10^8 CFU mL^{-1}.

2.9 *In vitro* synergistic MPTT/CDT antibacterial efficiency evaluation

Before antibacterial experiments, bacterial cultures of *E. coli* and *S. aureus* in the logarithmic phase (OD_{600} = 1.0) were washed three times with 0.9% saline solution to remove the bacterial culture medium. Then, bacterial pellets were collected by centrifugation and diluted by pH 5.5 PBS to have a bacterial density of 1×10^8 CFU mL^{-1}. Bacteria were divided into five different treated groups: Control, GNS/SiNR, GNS/SiNR+NIR, GNS@CP/SiNR and GNS@CP/SiNR+NIR. The concentration of the materials was 150 μg mL^{-1}, and irradiated with a 1064 nm laser (1 W cm^{-2}) for 5 min. To investigate the concentration-dependent antibacterial efficiency of GNS@CP/SiNR+NIR, materials with concentrations of 0, 50, 100, 150, and 200 μg mL^{-1} were added. After laser irradiation, bacteria were incubated in a 37 °C incubator for another 4 h. Then, the bacterial suspensions from different treatment groups were plated on agar plates and incubated overnight at 37 °C. The agar plate counting method by counting the bacterial colony numbers was used to determine the antibacterial efficiency of each treatment.

2.10 *In vitro* synergistic MPTT/CDT antibiofilm efficiency evaluation

2.10.1 Three-dimension confocal laser scanning microscopy (CLSM) assay. Firstly, 100 μL bacterial suspensions of *E. coli* and *S. aureus* at the logarithmic growth phase (OD_{600} = 1.0) were added to the 96-well plate and cultured in a 37 °C incubator for 48 h, during which the LB culture medium was replaced every 12 h to allow the bacteria to form dense biofilms. Then, biofilms were subjected to different treatments: control, GNS/SiNR, GNS/SiNR+NIR, GNS@CP/SiNR and GNS@CP/SiNR+NIR. The concentration of the materials was 150 μg mL^{-1} and irradiated with a 1064 nm laser (1 W cm^{-2}) for 5 min. After that, biofilms were further incubated at 37 °C for 12 h, followed by washing with PBS, and then stained by 3 μL SYTO-9 and PI fluorescent dyes (V/V = 1 : 1) in the dark for 30 min. Finally, the bacterial biofilms were washed with PBS to remove excess dye and observed using the LSM 880 confocal microscope.

2.10.2 Crystal violet staining assay. Similar to the above treatments, bacterial biofilms were firstly subjected to different treatments, then biofilms were fixed with 200 μL anhydrous methanol and stained by 1% crystal violet dye at 37 °C in the dark for 30 min. After washing several times with sterile PBS to remove excess dye, digital photographs of the crystal violet-stained biofilms in each well were recorded. After that, 200 μL anhydrous ethanol was added to each well and placed on a shaker for 15 min until the crystal violet was completely dissolved. Finally, the absorbance of the bacterial suspensions in each well at 570 nm was measured using a microplate reader.

2.11 Bacterial cell membrane integrity assay

2.11.1 CLSM assay. Briefly, bacteria (1×10^8 CFU mL^{-1}) were subjected to different treatments: control, GNS/SiNR, GNS/SiNR+NIR, GNS@CP/SiNR and GNS@CP/SiNR+NIR. The concentration of materials was 150 μg mL^{-1} and irradiated with a 1064 nm laser (1 W cm^{-2}) for 5 min. Then, 1 μL of STYO-9 and 1 μL of PI dye were both added to each group, and the mixture was incubated in the dark at 37 °C for 15 min. After that, the bacterial suspensions were centrifuged (5000 rpm, 3 min), washed twice with sterile PBS, and resuspended in 200 μL of

 This journal is © The Royal Society of Chemistry 2024

Published on 18 kwietnia 2024. Downloaded on 21.04.2026 23:01:02.

sterile PBS. Next, 50 μL of the bacterial suspension was added to a confocal dish and fixed. Finally, CLSM images of bacteria in each well was observed and recorded using a Zeiss LSM88 confocal microscope.

2.11.2 Cellular components leakage detection. After different treatments as above, the supernatant of the bacterial suspension was collected, filtered using a 0.22 μm filter membrane, and the optical density of the supernatant at 260 nm (OD_{260}) was measured using UV-Vis spectroscopy to determine the release level of the intracellular components.

2.12 Scanning electron microscopy (SEM) observation

After different treatments as above, the bacteria were fixed by 2.5% glutaraldehyde at 4 °C for 12 h. After centrifugation by removing glutaraldehyde, the bacteria were hydrated in a gradient of ethanol (30%, 50%, 70%, 80%, 90% and 100%) for 10 min. Finally, the bacteria were dropped onto a single-crystal silicon wafer, dried by supercritical CO_2 drying method, spayed with gold, and observed using the SEM apparatus to evaluate changes in the bacterial morphology.

2.13 Intracellular reactive oxygen species (ROS) detection

A DCFH-DA probe was used for detecting intracellular ROS of bacteria with different treatments. After the above treatments, bacteria were stained with 10 μM DCFH-DA for 30 min at 37 °C in the dark. Subsequently, a Hoechst 33342 fluorescent probe was added and incubated for another 30 min. Excess probes were removed by washing with 0.9% PBS. Finally, the fluorescence intensity of each bacterial suspension was measured using fluorescence spectroscopy. At the same time, bacterial suspensions were dropped onto the laser confocal dish for the CLSM assay.

2.14 Intracellular glutathione (GSH) assay

The GSH detection kit (ThiolTrace Violet 500, a fluorescent probe) was used for detecting the intracellular GSH of bacteria with different treatments. After the above treatments, 10 μM ThiolTrace Violet 500 probe was added to the bacterial suspensions and incubated at 37 °C in the dark for 30 min. After a complete rinse with PBS, bacterial suspensions were dropped onto the laser confocal dish for the CLSM assay. The fluorescence intensity of each CLMS image was semi-quantified using ImageJ software.

2.15 TUNEL assay

The DNA damage effect of different treatments was investigated using the TUNEL assay kit. Briefly, after the above treatments, bacterial suspensions were centrifuged and washed with PBS three times. Then, 200 μL PBS containing 10 μM TUNEL dye was added and incubated in the dark at 37 °C for 1 h. Finally, TUNEL-stained bacteria were observed by a Zeiss LSM88 confocal microscope.

2.16 *In vitro* cell viability assay

Mouse embryo fibroblasts (NIH/3T3) were used to evaluate the *in vitro* biocompatibility of GNS@CP/SiNR. Briefly, NIH/3T3 cells were seeded in a 96-well plate at a density of 5×10^3 cells per well in Dulbecco's modified Eagle's medium (DMEM). After cell adhesion, the medium was replaced with fresh cell culture medium containing GNS/SiNR or GNS@CP/SiNR with different concentrations and cultured for 24 h. Finally, the cell viability was assessed using the Cell Counting Kit-8 (CCK-8) assay kit.

2.17 *In vivo* antibacterial and wound healing effect of GNS@CP/SiNR

2.17.1 Establishment of the *S. aureus* infected full-thickness excision wound model. Twenty female SD rats (4 to 6 weeks old, the average body weight was 180 g) purchased from Beijing Vital River Laboratory Animal Technology Co., Ltd were randomly divided into 5 groups (4 rats/group): control, GNS/SiNR, GNS/SiNR+NIR, GNS@CP/SiNR and GNS@CP/SiNR+NIR. All animal experiments were conducted in accordance with the regulations of the Animal Experiment Ethics Committee of Jinan University. After anesthesia, a wound with a diameter of approximately 1.5 cm was created on the back of the rats through surgical procedures. The wounds were subsequently infected with 200 μL *S. aureus* at a concentration of 1×10^8 CFU mL^{-1} for 2 days.

2.17.2 *In vivo* photothermal effect of GNS@CP/SiNR. Briefly, a 200-μL GNS@CP/SiNR dispersion (150 μg mL^{-1}) was sprayed carefully onto the rats' infected wounds and irradiated by a 1064 nm laser (1 W cm^{-2}) for 5 min. Thermal images and temperature changes of the rats' wound areas were captured using a near-infrared thermal imaging camera (Fotric-220 s, China). Thermal images and temperature changes of the rats' wounds with PBS and 1064 nm laser-irradiated treatments were used as controls.

2.17.3 *In vivo* synergistic MPTT/CDT antibacterial evaluation. After 2 days infection, the rats' wounds were subjected to different treatments: control, GNS/SiNR, GNS/SiNR+NIR, GNS@CP/SiNR, and GNS@CP/SiNR+NIR. Every two days, treatment was administered by carefully dropping 150 μg mL^{-1} GNS/SiNR or GNS@CP/SiNR to the wounds, followed by irradiating with a 1064 nm laser (1 W cm^{-2}) for 5 min. On days 0, 3, 5, 7, and 10, the exudate from the rats' wounds were collected, diluted with PBS, and evenly spread on the LB agar plates. The plates were then incubated at 37 °C in a biological incubator overnight. Finally, the bacterial colonies on each agar plate were photographed using a digital camera, and ImageJ software was used to count the number of bacterial colonies to evaluate the antibacterial effect of different treatments.

2.17.4 Wound healing efficiency evaluation. After the above treatments, the photographs of the wounds on days 0, 2, 4, 6, 8, and 10 were carefully recorded. Then, the wound area of each group was measured and analyzed using the ImageJ software.

2.17.5 Rat body weight evaluation. The rats' body weight in each group was recorded every 2 days to assess the safety of GNS@CP/SiNR and the corresponding treatments.

2.17.6 Histological analysis. At the end of treatment, rats were euthanized and the skin tissues surrounding the infected wound were removed, fixed by 4% paraformaldehyde, embedded

Published on 18 kwietnia 2024. Downloaded on 21.04.2026 23:01:02.

in paraffin, and histological slices were prepared. Tissue sections were stained with H&E and Masson for histopathological analysis, and the thickness of the dermis in the rats' wound tissues were determined using ImageJ software. Inflammatory factors of TNF-α and IL-6, and newly formed blood vessel indicators of α-SMA and CD31 were detected by performing the immunofluorescent staining assay. The semi-quantitative analysis of the fluorescence intensity in the immunofluorescent histological images was performed by ImageJ software.

2.18 In vivo biocompatibility evaluation

2.18.1 Histological analysis. At the end of the treatment, the rats were euthanized, and the heart, liver, spleen, lungs, and kidneys were collected. After multiple washes with PBS to remove residual blood from the organ sites, the organs were fixed in 4% paraformaldehyde, then embedded in paraffin, sectioned, and stained with H&E. The H&E images of the rats' organs were taken using an inverted optical microscope.

2.18.2 Blood biochemical analysis. At the end of the treatment, the rats were anesthetized, and blood was collected from the eye vein and placed in anticoagulant blood collection tubes for blood routine analysis.

2.19 Statistical analysis

All data were presented as mean ± standard deviation, and analyzed for differences between different groups using One-way ANOVA in GraphPad 8.3 software. The significance of differences was determined based on P values, where * indicates $P < 0.05$, ** indicates $P < 0.001$, and *** indicates $P < 0.0001$.

3. Results and discussion

3.1 Synthesis and Characterization of the GNS@CP/SiNR Janus nanostructure

In the present work, the copper peroxide (CP) nanodots decorated gold nanostar (GNS)/silica nanorod (SiNR) Janus nanostructure (GNS@CP/SiNR) was rationally designed and fabricated, and displayed excellent near-infrared (NIR)-II photothermal and self-activated hydrogen radical (•OH) generation properties for the highly-efficient treatment of wound infections. Specifically, the GNS@CP/SiNR Janus nanostructure was prepared using a modified seed-mediated synthetic method.[9] Firstly, spherical gold nanoparticles (Au NPs) were bound to the thiolated SiNR (SiNR-SH) to form the Au NPs/SiNR nanocomposite *via* the specific Au–S bond. Then, Au NPs in Au NPs/SiNR served as the seeds and subsequently grew to gold nanostars in the seed-growth medium by forming the GNS/SiNR Janus nanostructure, where one SiNR was bound with one gold nanostar. Finally, copper peroxide specifically grew on the surface of the gold nanostar during the *in situ* growth process, obtaining the GNS@CP/SiNR Janus nanostructure. The whole synthetic process was monitored by TEM measurement, where the structure of SiNR, Au NPs/SiNR, GNS/SiNR and GNS@CP/SiNR could be clearly seen (Fig. 1A and Fig. S1, ESI†). Dynamic

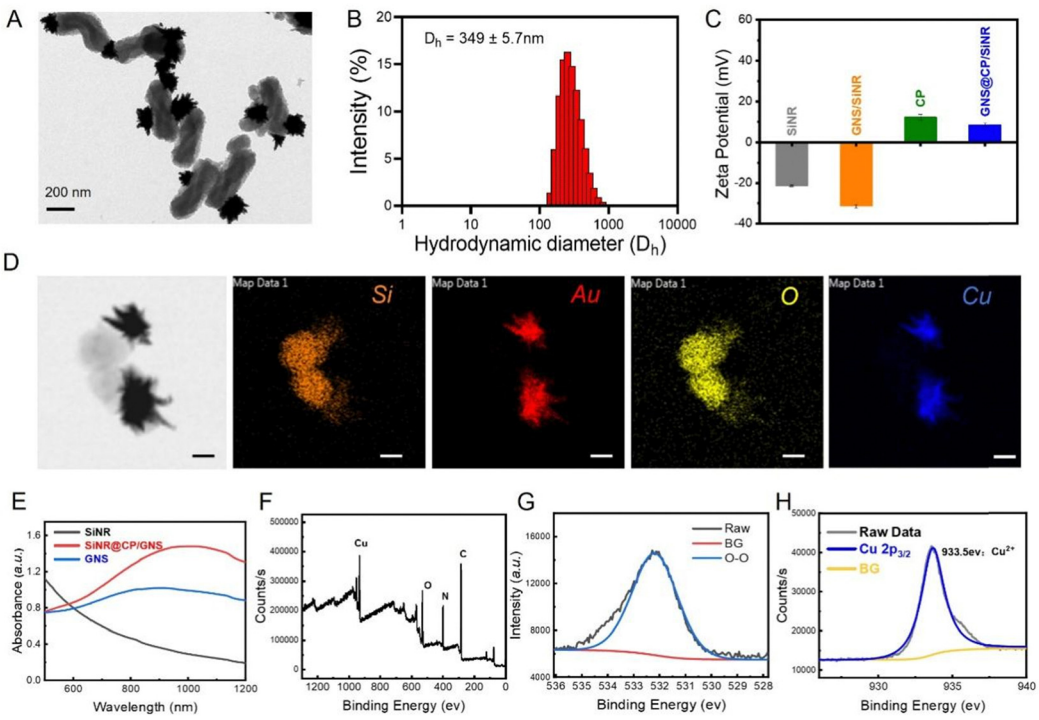

Fig. 1 Characterization of the GNS@CP/SiNR Janus nanostructure. (A) TEM image of the GNS@CP/SiNR Janus nanostructure, scale bar represents 200 nm. (B) Intensity-weighted size distribution of the GNS@CP/SiNR Janus nanostructure. (C) Zeta potentials of SiNR, GNS/SiNR, CP and the GNS@CP/SiNR Janus nanostructure. (D) Elemental mapping image of GNS@CP/SiNR. (E) UV-Vis-NIR spectra of SiNR, GNS and SiNR@CP/GNS. (F) Survey XPS spectrum of GNS@CP/SiNR and high-resolution XPS spectra of O 1s (G) and Cu 2p (H).

 This journal is © The Royal Society of Chemistry 2024

Published on 18 kwietnia 2024. Downloaded on 21.04.2026 23:01:02.

laser scattering (DLS) measurements were also performed to monitor changes in the hydrodynamic diameter and zeta potential value of the nanosystem during the whole synthetic process. The DLS measurement results showed that the hydrodynamic diameter (D_h) of the nanosystem increased from 307.8 ± 7.3 nm (SiNR) to 349.3 ± 5.7 nm (GNS@CP/SiNR) (Fig. 1B and Fig. S2, ESI†), and the zeta potential of the nanosystem increased from −20 mV (SiNR) to +8.6 mV (GNS@CP/SiNR) (Fig. 1C), suggesting the successful preparation of GNS@CP/SiNR. Elemental imaging data further confirmed the Janus nanostructure of the prepared GNS@CP/SiNR, where Si, Au, O and Cu elements could be clearly observed (Fig. 1D). Upon the preparation of GNS@CP/SiNR, a strong surface plasmonic resonance (SPR) absorption band at approximately 1064 nm (NIR-II region) could be observed (Fig. 1E). This must be due to the formation of the particular Janus nanostructure, since SiNR and CP alone did not show a typical SPR peak, and GNS only displayed a typical SPR peak at approximately 808 nm (NIR-I region). This indicated that GNS@CP/SiNR is a potent NIR-II photothermal material for safe biomedical applications. To further confirm the presence of CP nanodots in GNS@CP/SiNR, X-ray photoelectron spectroscopy (XPS) was performed to detect the valence states of copper and oxygen. As shown in Fig. 1F, both Cu and O elements could be found in the survey XPS spectra of GNS@CP/SiNR. The high-resolution O 1s XPS spectrum showed a characteristic peak at 532.5 eV (Fig. 1G), which was assigned to the O–O group, suggesting that the valence state of O in CP was −1. The high-resolution Cu 2p XPS spectrum displayed a typical peak at 933.5 eV (Fig. 1H), indicating that the valence state of

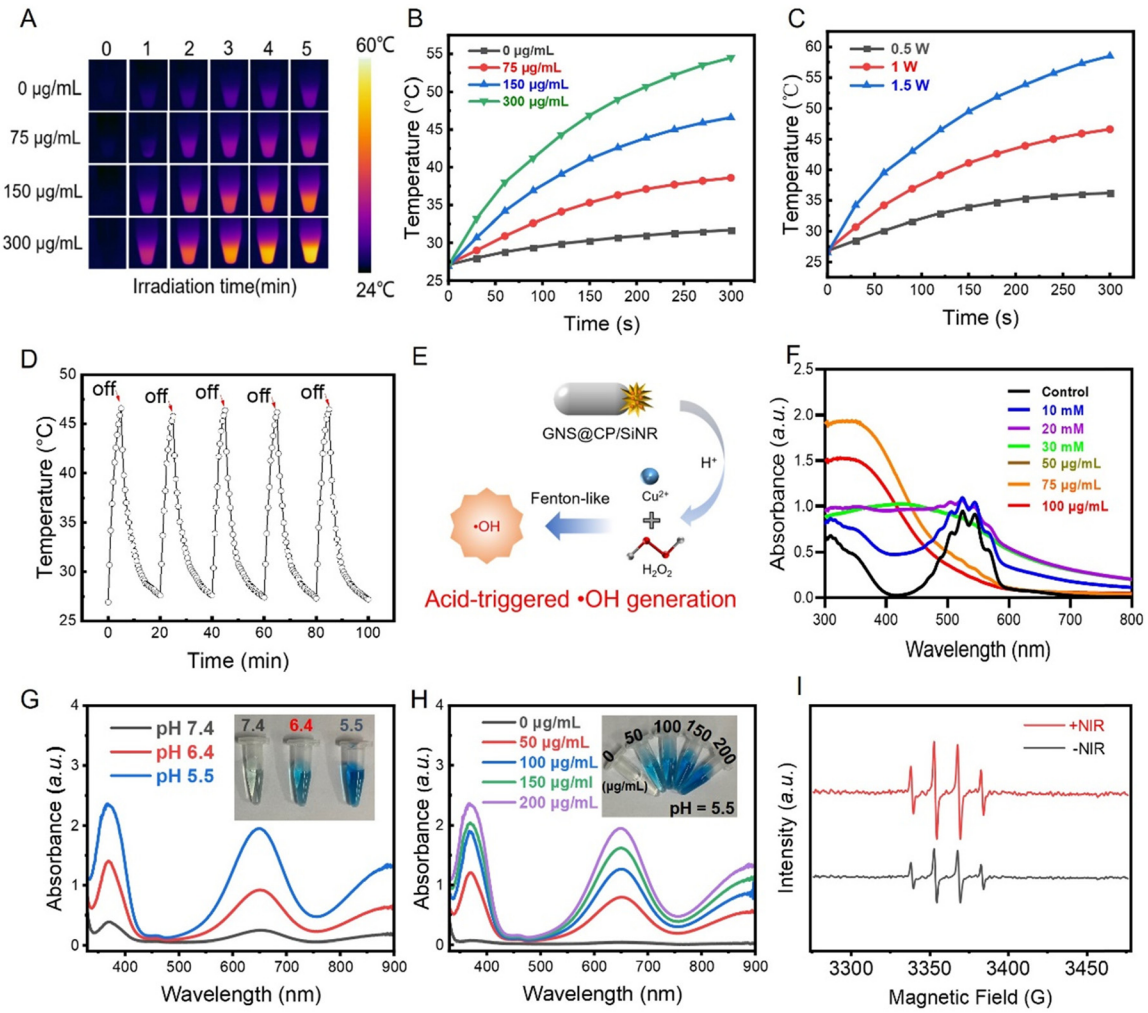

Fig. 2 Characterization of the NIR-II photothermal and •OH generation properties of the GNS@CP/SiNR Janus nanostructure. (A) Thermal images showing the photothermal effect of GNS@CP/SiNR with different concentrations under 1064 nm laser irradiation (1.0 W cm^{-2}). (B) Photothermal effect of GNS@CP/SiNR with different concentrations. (C) Photothermal effect of GNS@CP/SiNR under different laser power density irradiation conditions. (D) Photothermal stability of GNS@CP/SiNR. (E) Scheme shows the acid-triggered •OH generation property of GNS@CP/SiNR. (F) UV-Vis spectra of the $KMnO_4$ solution with the addition of 10–30 mM H_2O_2 and GNS@CP/SiNR with different concentrations. (G) UV-Vis spectra of TMB solutions treated with GNS@CP/SiNR in different pH values. Insert is an image showing the TMB color in different pH conditions. (H) UV-Vis spectra of TMB solutions treated with GNS@CP/SiNR of different concentrations in pH 5.5 condition. Insert is an image showing the TMB color in different concentrations. (I) ESR spectra of GNS@CP/SiNR with DMPO addition in both NIR and non-NIR irradiation conditions.

Published on 18 kwietnia 2024. Downloaded on 21.04.2026 23:01:02.

Cu CP was +2. The XPS results confirmed the successful decoration of the CP nanodots on GNS@CP/SiNR. The XRD spectrum displayed all of the typical XRD patterns of SiNR, GNS and CP, demonstrating the successful preparation of GNS@CP/SiNR (Fig. S3, ESI†). Moreover, the colloidal stability of the GNS@CP/SiNR dispersion was also evaluated by monitoring its changes in D_h and the zeta potential over a period of 48 h. It showed that D_h of GNS@CP/SiNR was maintained at approximately 350 nm, and the zeta potential was kept in the range of +7 mV to +8 mV in 48 h (Fig. S4, ESI†), suggesting the excellent stability of GNS@CP/SiNR.

3.2 NIR-II photothermal and •OH generation properties of GNS@CP/SiNR

Because GNS@CP/SiNR displayed a strong SPR absorption band in the NIR-II region, its photothermal effect upon 1064 nm laser irradiation was evaluated. Thermal imaging data indicated the time and concentration-dependent photothermal effects of GNS@CP/SiNR (Fig. 2A and B). The temperature of the nanosystem gradually increased with the irradiation time. Tuning the laser power density can also control the photothermal behavior of GNS@CP/SiNR. Generally, increasing the laser power density resulted in a stronger photothermal effect of the nanosystem (Fig. 2C). In particular, we found that GNS@CP/SiNR exhibited a mild-photothermal effect by increasing the temperature to approximately 45 °C within 5 min under conditions of 1 W cm^{-2} laser power density and materials concentration of 150 μg mL^{-1} (Fig. 2A and B). This indicated that GNS@CP/SiNR is a potential material for mild photothermal therapy (MPTT). By further calculation, the photothermal conversion efficiency of GNS@CP/SiNR was determined to be 32.3%. Moreover, GNS@CP/SiNR displayed a stable photothermal conversion efficiency as its photothermal effect remained unchanged after 5 cycles of 1064 nm laser irradiation-cooling processes (Fig. 2D). CP is a type of Fenton-like reagent with an acid-triggered •OH generation property. Specifically, upon exposure to acidic conditions, CP can responsively dissociate by releasing Cu^{2+} and H_2O_2, which can subsequently transform into •OH *via* the Fenton-like catalytic reaction (Fig. 2E). The acidic pH-responsive Cu^{2+} release profile was monitored by performing ICP-AES measurements. It is clear that the Cu^{2+} release rate was significantly enhanced in acidic pH conditions (Fig. S5, ESI†). Then, the acid-activated H_2O_2-producing property of GNS@CP/SiNR was investigated using the $KMnO_4$-based colorimetric assay. In the presence of H_2O_2, the pink $KMnO_4$ solution was gradually reduced, which was accompanied by the decrease in the UV-Vis absorption value at the wavelength range of 500 nm to 600 nm. As it was shown, the addition of 30 mM H_2O_2 caused the complete fading of the pink $KMnO_4$ solution. UV-Vis absorption peaks in the range from 500 nm to 600 nm disappeared as well (Fig. 2F and G), suggesting the complete reduction of $KMnO_4$ by H_2O_2. A similar phenomenon was observed to that of GNS@CP/SiNR with a concentration of 100 μg mL^{-1}, which made the pink $KMnO_4$ solution become colorless and caused the disappearance of the UV-Vis absorption peaks (Fig. 2F and Fig. S6, ESI†). By comparison, it was estimated that 100 μg mL^{-1} GNS@CP/SiNR could self-supply approximately 30 mM H_2O_2 under acidic conditions. The acidic pH-responsive H_2O_2 release profile was also investigated, as shown in Fig. S7 (ESI†). It showed that a higher level of H_2O_2 was generated in acidic pH conditions. The produced H_2O_2 can further react with the released Cu^{2+} to generate •OH, which can be detected using the commonly used 3,3′,5,5′-tetramethylbenzidine (TMB) assay. In the presence of •OH, the transparent TMB can be oxidized to blue oxTMB, displaying a typical UV-Vis absorption peak at 650 nm. As it was shown (Fig. 2G), the color of the TMB solution only slightly changed in neutral conditions. It turned into a blue color at pH 6.4, and changed into a dark blue color at pH 5.5, suggesting the acid-triggered •OH generation property of GNS@CP/SiNR. UV-Vis measurements further confirmed that •OH can be generated under acidic conditions, as an obvious absorption peak at 650 nm could be observed in both pH 5.5 and pH 6.4 conditions (Fig. 2G). Moreover, a concentration-dependent •OH generation behavior was observed for GNS@CP/SiNR. A higher concentration of materials led to a higher •OH generation level in acidic environments, while negligible •OH could be detected under the pH 7.4 condition (Fig. 2H and Fig. S8, S9, ESI†). The •OH generation was also confirmed by ESR measurements using 5,5-dimethyl-1-pyrroline-*N*-oxide (DMPO) as the trapping agent. Typical DMPO/•OH adduct signals were observed in the ESR spectra (Fig. 2I). Interestingly, it was shown that the NIR laser irradiation could further enhance the •OH generation level as stronger ESR signals were observed. In all, GNS@CP/SiNR displayed excellent NIR-II mild photothermal effect and self-activated •OH generation in acidic environments, exhibiting promising use for antibacterial applications *via* the synergistic MPTT/CDT effect.

3.3 *In vitro* synergistic MPTT/CDT antibacterial efficiency of GNS@CP/SiNR

Next, the antibacterial activity of GNS@CP/SiNR against both Gram-negative *Escherichia coli* (*E. coli*) and Gram-positive *Staphylococcus aureus* (*S. aureus*) was investigated using the agar plate counting method. As it was shown, controls of the NIR-II 1064 nm laser and GNS/SiNR did not show any antibacterial effect against both bacteria (Fig. 3A). The mild photothermal effect of GNS/SiNR (GNS/SiNR+NIR) clearly reduced the bacterial colony numbers, and the •OH generated by GNS@CP/SiNR also caused a significant decrease in bacterial viability (Fig. 3B and Fig. S10, ESI†). Remarkably, GNS@CP/SiNR+NIR treatment completely eliminated both *E. coli* and *S. aureus* due to its synergistic MPTT/CDT antibacterial effect (Fig. 3B and Fig. S10, ESI†). A concentration-dependent antibacterial activity of GNS@CP/SiNR was also observed. As the concentration of the materials increased, the antibacterial efficiency of GNS@CP/SiNR against both *E. coli* and *S. aureus* was enhanced (Fig. 3C and E). In particular, when the concentration of the materials increased to 200 μg mL^{-1}, the synergistic MPTT/CDT antibacterial effect of GNS@CP/SiNR resulted in the complete elimination of both bacteria (Fig. 3D and F).

 This journal is © The Royal Society of Chemistry 2024

Published on 18 kwietnia 2024. Downloaded on 21.04.2026 23:01:02.

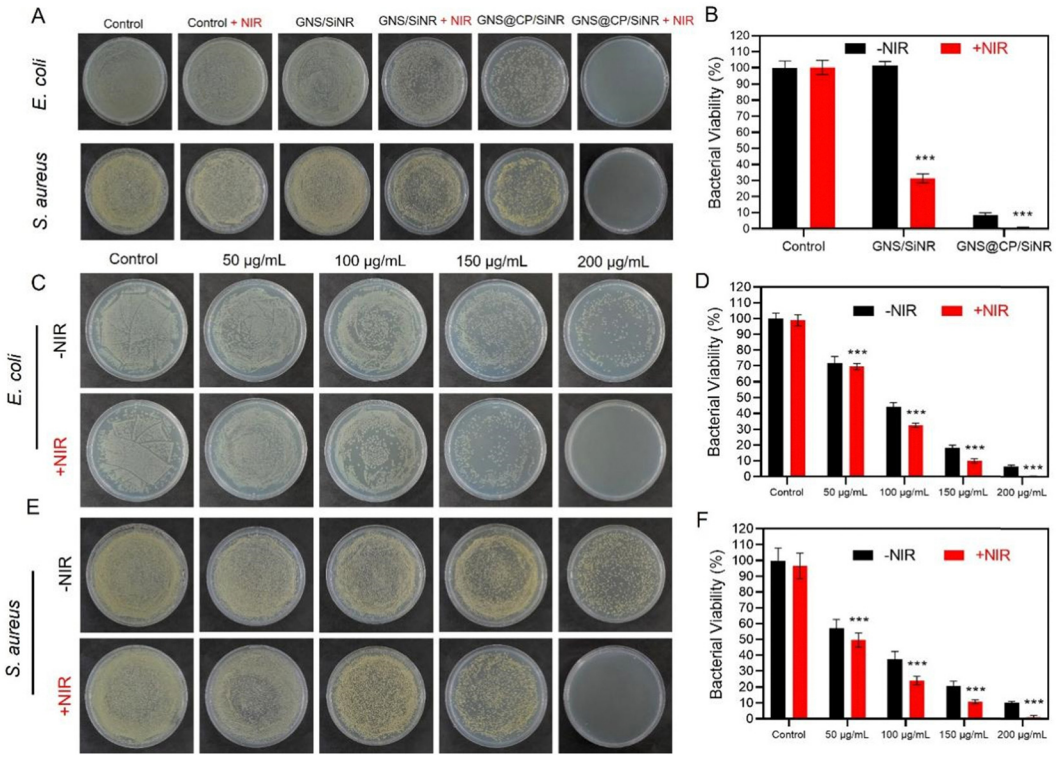

Fig. 3 The synergistic MPTT/CDT antibacterial effect of GNS@CP/SiNR. (A) Agar plate images showing the antibacterial activity of different treatments against *E. coli* and *S. aureus*. (B) Histogram showing the antibacterial efficiency of different treatments against *S. aureus*. (C) Agar plate images showing the antibacterial activity of GNS@CP/SiNR against *E. coli* with different concentrations under laser or non-laser irradiation conditions, and the corresponding antibacterial efficiency histogram (D). Agar plate images showing the antibacterial activity of GNS@CP/SiNR against *S. aureus* with different concentrations under laser or non-laser irradiation conditions (E), and the corresponding antibacterial efficiency histogram (F).

3.4 *In vitro* synergistic MPTT/CDT antibiofilm efficiency of GNS@CP/SiNR

The synergistic MPTT/CDT antibiofilm efficiency of GNS@CP/SiNR was also evaluated by performing crystal violet staining assay and three-dimension confocal laser scanning microscopy (CLSM) measurements. Similar to the above antibacterial results, GNS@CP/SiNR exhibited robust biofilm-eradication ability upon 1064 nm laser irradiation. The crystal violet staining assay results showed that MPTT (GNS/SiNR+NIR) or CDT (GNS@CP/SiNR) alone led to lower density of *S. aureus* biofilm as compared with that of the controls (Fig. 4A and Fig. S11, ESI†). As expected, the synergistic MPTT/CDT effect displayed the strongest antibiofilm activity, as almost no crystal violet-stained *S. aureus* biofilm could be observed after GNS@CP/SiNR+NIR treatment (Fig. 4A). The biofilm biomass of *S. aureus* in each group after different treatments was also detected by measuring the optical value of the remanent biofilm at 570 nm (OD_{570}). It showed that GNS@CP/SiNR+NIR treatment led to the lowest OD_{570} value (Fig. 4B and Fig. S11, ESI†). A materials concentration-dependent biofilm-eradication effect was found for GNS@CP/SiNR. The preformed *S. aureus* biofilm could be completely eliminated by the synergistic MPTT/CDT effect at the concentration of 200 μg mL^{-1}, where a negligible violet color and lowest OD_{570} value were observed (Fig. 4C, D and Fig. S11, ESI†). In the CLSM measurements, the SYTO-9/PI dual-florescent staining method was used, where live bacteria were stained by the green fluorescent SYTO-9 dye and dead bacteria were stained by the red fluorescent PI dye (Fig. 4E). Similarly, MPTT caused partial damage to the *S. aureus* biofilm, as a small portion of red fluorescence could be visualized upon GNS/SiNR+NIR treatment (Fig. 4E and F). The CDT effect triggered significant damage to the *S. aureus* biofilm, where a large portion of red fluorescence was observed upon GNS@CP/SiNR treatment (Fig. 4E and F). Remarkably, the GNS@CP/SiNR+NIR treatment resulted in the highest red/green fluorescence ratio, suggesting the strongest biofilm-damage activity of the synergistic MPTT/CDT effect (Fig. 4E and F). Similar trends were also found for the *E. coli* biofilm (Fig. S12, ESI†).

3.5 The synergistic MPTT/CDT antibacterial mechanism of GNS@CP/SiNR

Next, the synergistic MPTT/CDT antibacterial mechanism of GNS@CP/SiNR was investigated. In order to exert an antibacterial effect, materials have to penetrate the bacterial membrane barrier. Therefore, the bacterial membrane-damage effect of GNS@CP/SiNR was firstly examined. The bacterial membrane integrity was monitored by the SYTO-9/PI dual-florescence staining assay, where bacteria with intact membranes were stained by the green fluorescent SYTO-9 dye and bacteria with damaged membranes can be stained by the red fluorescent PI dye. As shown in Fig. 5A, negligible red fluorescence could be visualized in the CLSM images of the control and

Published on 18 kwietnia 2024. Downloaded on 21.04.2026 23:01:02.

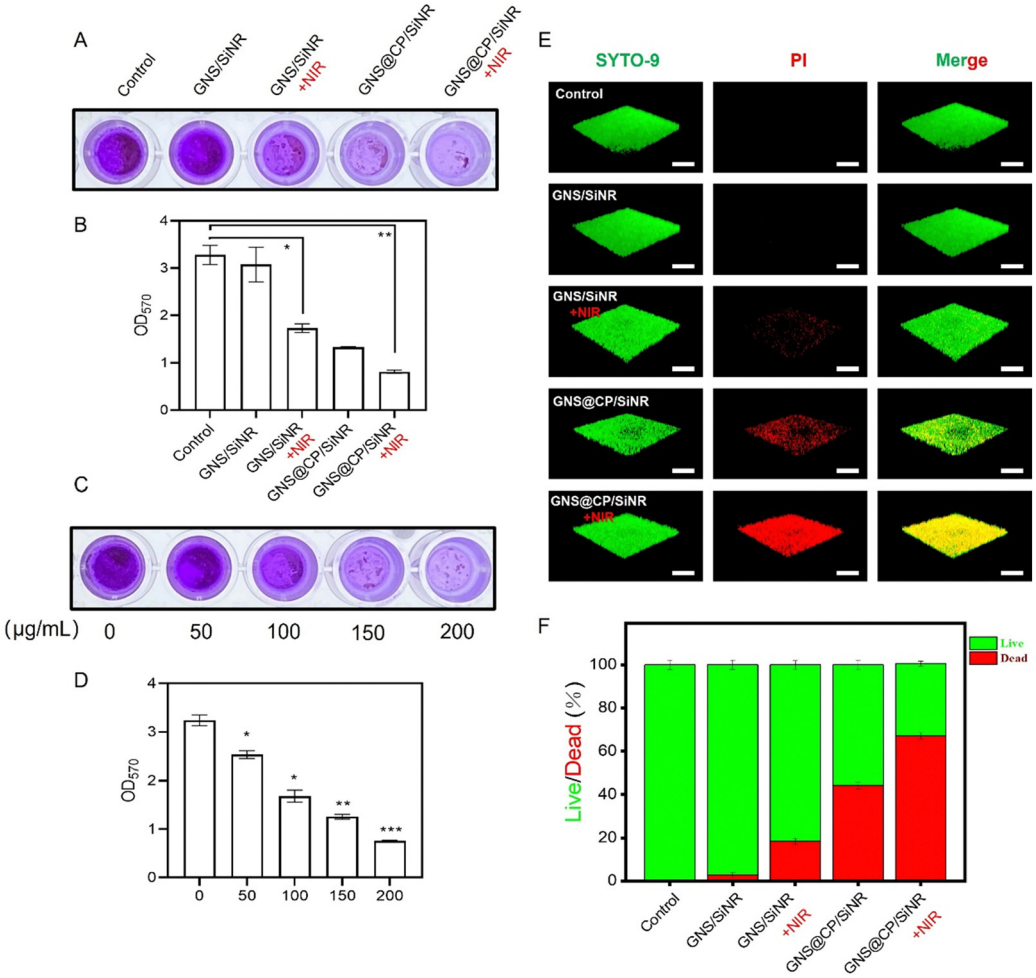

Fig. 4 The synergistic MPTT/CDT antibiofilm effect of GNS@CP/SiNR. (A) Crystalline violet-stained *S. aureus* biofilm after different treatments and the corresponding OD_{570} values (B). (C) Crystalline violet-stained *S. aureus* biofilm that has undergone GNS@CP/SiNR+NIR treatment with different concentrations and the corresponding OD_{570} values (D). (E) CLSM images of the *S. aureus* biofilm stained with SYTO-9/PI dual fluorescent dyes after different treatments, and the corresponding histogram (F) showing the percentage of live/dead bacteria. Scale bar represents 20 μm.

GNS/SiNR-treated groups, suggesting the non-membrane damage ability of GNS/SiNR. GNS/SiNR+NIR treatment caused an obvious red fluorescence in the CLSM images, indicating that MPTT could cause a certain degree of membrane damage to *E. coli* and *S. aureus*. A higher percentage of red fluorescence could be found in the GNS@CP/SiNR-treated groups (Fig. 5A and Fig. S13, ESI†), indicating that CDT triggered the stronger bacterial membrane-damage effect than MPTT. Intriguingly, the GNS@CP/SiNR+NIR treatment resulted in the highest level of red fluorescence (Fig. 5A and Fig. S13, ESI†), indicating that the *E. coli* and *S. aureus* membranes were severely destroyed by the synergistic MPTT/CDT damage effect. Scanning electron microscopy (SEM) measurements were performed to further confirm the bacterial membrane-destruction effect of GNS@CP/SiNR (Fig. 5B). In the control groups, *E. coli*/*S. aureus* exhibited regular rod/spherical morphology with smooth membranes. Similarly, the MPTT effect (GNS/SiNR+NIR) induced partial bacterial membrane breakage, while the CDT effect (GNS@CP/SiNR) caused more severe bacterial membrane damage, as demonstrated by the bacterial shape shrinkage and rough membrane surface. As expected, the MPTT and CDT effects synergistically triggered the complete rupture of the bacterial membrane, further demonstrating the robust membrane-breaking ability of the GNS@CP/SiNR treatment. Bacterial membrane damage can also lead to the efflux of intracellular components, such as DNA, RNA, or other functional proteins, which can be quantified by measuring the optical density value at 260 nm wavelength (OD_{260}).[31,32] Consistent with the above results, MPTT and CDT alone did trigger the leakage of intracellular components, as the OD_{260} values clearly increased in comparison with the control groups (Fig. 5C and E). The GNS@CP/SiNR+NIR treatment resulted in the highest level of OD_{260}, confirming the most severe damage effect of the synergistic MPTT/CDT effect (Fig. 5C and E). Moreover, a concentration-dependent bacterial membrane-damage effect was observed for GNS@CP/SiNR. Higher concentrations of the materials led to a higher OD_{260} level (Fig. 5D and F).

Bacterial membrane damage further facilitates the entrance of antibacterial materials, which can subsequently inactivate bacteria by causing an oxidative stress effect. Herein, the intracellular reactive oxygen species (ROS) were detected using

 This journal is © The Royal Society of Chemistry 2024

Published on 18 kwietnia 2024. Downloaded on 21.04.2026 23:01:02.

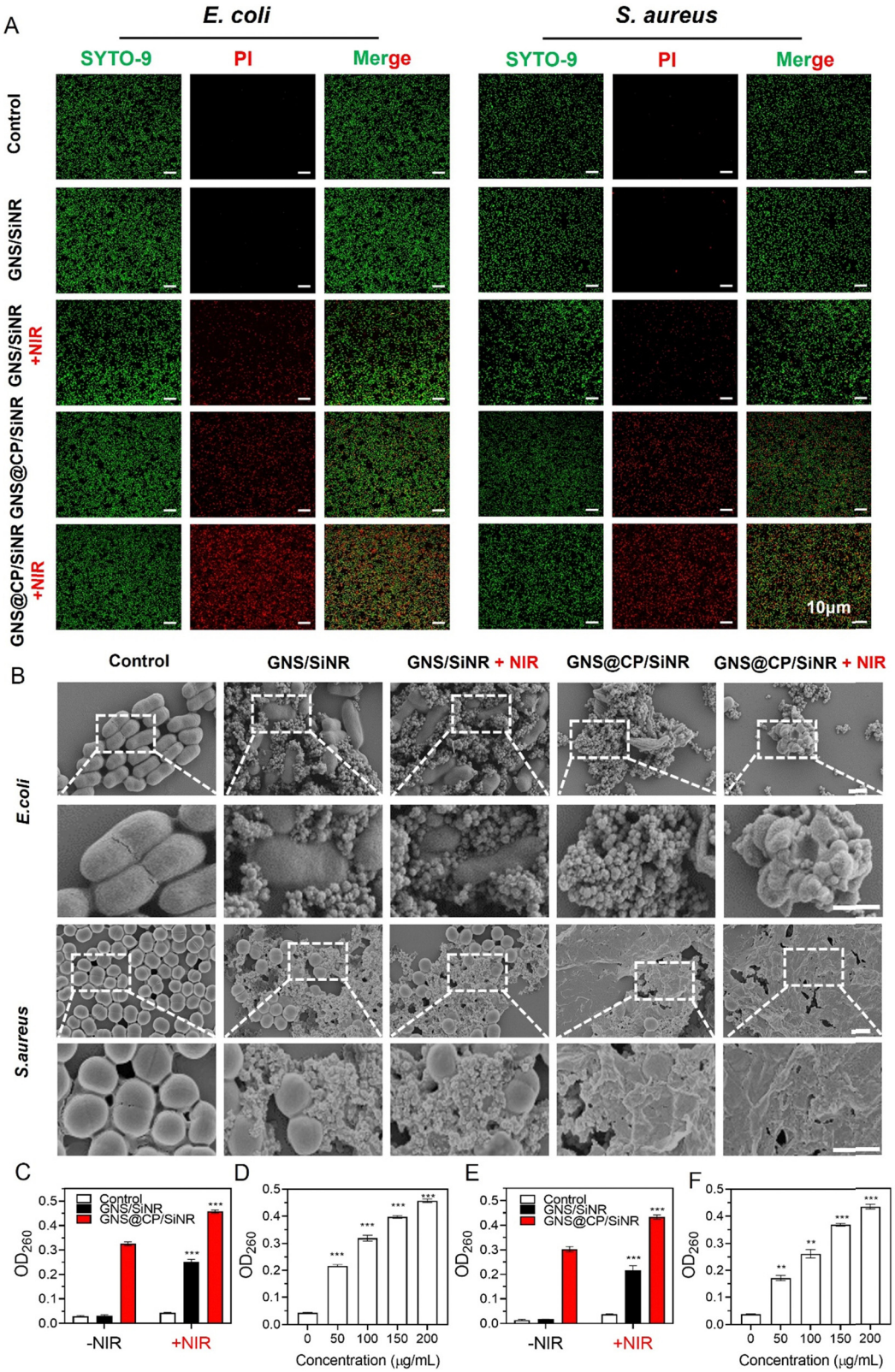

Fig. 5 The synergistic MPTT/CDT membrane damage effect of GNS@CP/SiNR. (A) CLSM images of *E. coli* and *S. aureus* stained with SYTO-9/PI dual fluorescent dyes after different treatments (scale bar represents 10 μm). (B) SEM images of *E. coli* and *S. aureus* after different treatments (scale bar represents 1 μm). OD_{260} of the supernatants extracted from *E. coli* (C) and *S. aureus* (E) after different treatments. OD_{260} of the supernatants extracted from *E. coli* (D) and *S. aureus* (F) treated by GNS@CP/SiNR+NIR with varied material concentrations.

Published on 18 kwietnia 2024. Downloaded on 21.04.2026 23:01:02.

2,7-dichlorodihydrofluorescein diacetate (DCFH-DA) as the fluorescent probe. In the presence of ROS, the non-fluorescent DCFH-DA can be oxidized to the green fluorescent DCF, which can be either observed by CLSM measurement or detected by fluorescence spectrophotometer with excitation/emission wavelengths of 488 nm/525 nm. CLSM images showed that GNS/SiNR+NIR treatment resulted in the appearance of some green fluorescent spots, indicating that the MPTT effect triggered moderate ROS generation inside both bacteria (Fig. S14 and S15, ESI†). In contrast, the GNS@CP/SiNR treatment led to an intense green fluorescence in the CLSM images (Fig. S14 and S15, ESI†), indicating that substantial ROS was induced by the CDT effect. This is in line with the previous findings, where it was reported that $^{\bullet}OH$ was able to induce severe oxidative stress to bacteria by boosting ROS production.[29] Interestingly, the GNS@CP/SiNR+NIR treatment caused the most intense green fluorescence intensity in the CLSM images, suggesting that the synergistic MPTT/CDT effect triggered the highest level of ROS generation among all the groups (Fig. 6A). The fluorescence spectrophotometer measurements further confirmed the above trends. The MPTT effect induced only a small fluorescent peak at 525 nm, while the CDT effect resulted in a strong fluorescent peak at 525 nm (Fig. 6B and C). The synergistic MPTT/CDT effect led to the strongest fluorescent peak at 525 nm (Fig. 6B and C). Glutathione (GSH) is a highly active ROS scavenger that protects bacteria from oxidative stress damage. Depletion of GSH can further augment the antibacterial activity of ROS.[33] Therefore, the intracellular GSH level was also detected using the ThiolTrace Violet 500 fluorescent probe. As shown in Fig. 6D and E, the MPTT effect caused a decrease in the GSH level to some degree, and the CDT effect greatly reduced the GSH content inside *S. aureus*. Combinational MPTT and CDT treatments displayed the most significant GSH depletion effect by almost completely eliminating GSH in *S. aureus*. Similar trends were also observed for *E. coli* (Fig. S16, ESI†). Because the bacterial nucleoplasm is the main target of ROS, the DNA damage effect of GNS@CP/SiNR was investigated by the terminal deoxynucleotidyl transferase-mediated dUTP nick-end labeling (TUNEL) assay (Fig. 6F, G and Fig. S17, ESI†). TUNEL staining images

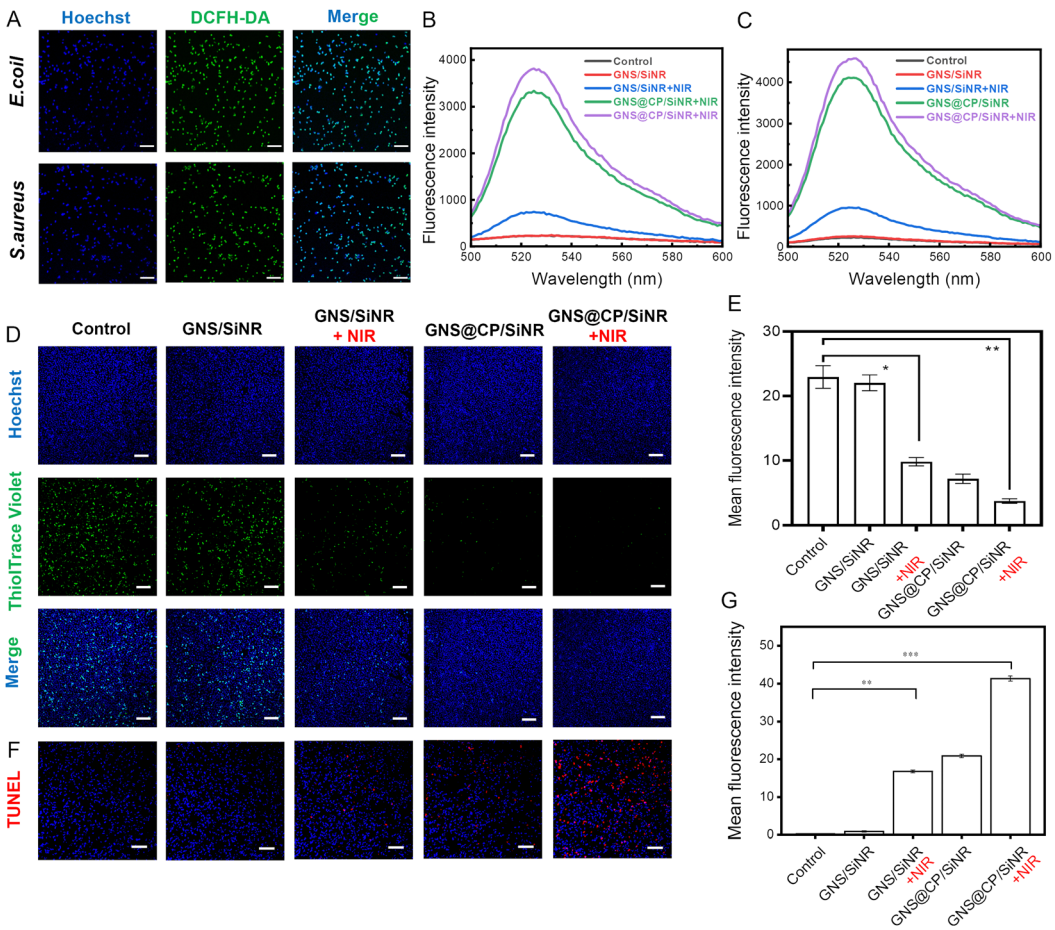

Fig. 6 The synergistic MPTT/CDT antibacterial mechanism of GNS@CP/SiNR. (A) CLSM images of *E. coli* and *S. aureus* stained by DCFH-DA fluorescent dye showing the intracellular ROS level after GNS@CP/SiNR+NIR treatment, and the corresponding fluorescence spectra of *E. coli* (B) and *S. aureus* (C). (D) CLSM images of *S. aureus* stained by the ThiolTrace Violet 500 fluorescent probe after different treatments and the corresponding mean fluorescence intensity (E). (F) CLSM images of TUNEL-stained *S. aureus* after different treatments, and the corresponding mean fluorescence intensity (G). Scale bar represents 10 μm.

 This journal is © The Royal Society of Chemistry 2024

Published on 18 kwietnia 2024. Downloaded on 21.04.2026 23:01:02.

exhibited that the MPTT or CDT effect alone indeed induced partial DNA damage, while the synergistic MPTT/CDT effect significantly triggered the cleavage of bacterial DNA.

Taken together, a possible synergistic MPTT/CDT antibacterial mechanism of GNS@CP/SiNR was proposed, as shown in Scheme 1. Firstly, the positive surface of GNS@CP/SiNR facilitated their anchoring to the negative bacterial membrane through electrostatic interaction. Upon NIR-II 1064 nm laser irradiation, the MPTT and CDT effects synergistically damaged the bacterial membrane by accelerating the intracellular protein components' release and enhancing the penetration of GNS@CP/SiNR. As followed, intracellular ROS generation was boosted *via* severe oxidative stress effect, which subsequently caused the depletion of intracellular GSH and induced DNA damage, finally leading to the death of bacteria.

3.6 *In vivo* synergistic MPTT/CDT antibacterial and wound healing efficiency of GNS@CP/SiNR

Due to the excellent *in vitro* antibacterial and biofilm-eradication outcomes of GNS@CP/SiNR, the *in vivo* synergistic MPTT/CDT effect of GNS@CP/SiNR was investigated on the *S. aureus*-infected full thickness excision wound rat model (Fig. 7A). Firstly, the *in vivo* MPTT effect was evaluated using thermal imaging assays. As shown in Fig. 7B, the temperature of the rats' wound tissue rarely increased under 1064 nm laser irradiation, while the temperature clearly increased in those with GNS/SiNR and GNS@CP/SiNR treatments. In particular, the temperature of the GNS@CP/SiNR treated rats' wound tissues increased to about 47.8 °C upon 5 min laser irradiation (Fig. 7C), further confirming the *in vivo* MPTT effect of GNS@CP/SiNR. Then, the *in vivo* antibacterial efficiency was evaluated using the agar plate counting method. It clearly showed that the bacterial colony numbers in the GNS/SiNR+NIR, GNS@CP/SiNR and GNS@CP/SiNR+NIR-treated wounds started to decrease on Day 3 (Fig. S18, ESI†). After 10 days treatment, the remanent *S. aureus* in the GNS/SiNR+NIR and GNS@CP/SiNR-treated wounds decreased sharply to 36% and 12%, respectively (Fig. 7D and G). Remarkably, the GNS@CP/SiNR+NIR treatment almost led to the complete elimination of the infected *S. aureus* in the rats' wound (Fig. 7G), demonstrating the robust antibacterial effect of the combinational MPTT and CDT treatments. Bacterial clearance can relieve the inflammation microenvironment of the rats' wounds, which in turn further promotes the wound-healing process.[34] As shown in Fig. 7E, F and H, the rats' wounds that underwent GNS/SiNR+NIR, GNS@CP/SiNR and GNS@CP/SiNR+NIR treatments displayed better healing outcomes than those of the controls. On Day 10, almost complete wound closure was visualized for rats with GNS@CP/SiNR+NIR treatment (Fig. 7E and F), suggesting the excellent wound healing activity of the combined MPTT and CDT treatments. Histological sections of wound tissues with hematoxylin and eosin (H&E) staining were also analyzed to study the antibacterial and wound healing effect of GNS@CP/SiNR (Fig. 7I). H&E images showed that obvious neutrophil infiltration in the skin tissues of the control groups, while this phenomenon was largely relieved in the GNS/SiNR+NIR and GNS@CP/SiNR-treated tissues, suggesting that skin tissue inflammation could be greatly improved by the MPTT or CDT effect. As expected, negligible inflammatory cells could be found in the H&E images with GNS@CP/SiNR+NIR treatment, indicating that the skin tissue inflammation was completely eliminated by the synergistic MPTT/CDT effect. The collagen deposition in the skin wound tissues were also examined by Masson staining assay. Consistently, the synergistic MPTT/CDT effect resulted in the highest collagen deposition density in the skin wound tissues (Fig. 7J and K).

As followed, the synergistic MPTT/CDT anti-inflammation and wound-healing mechanisms of GNS@CP/SiNR were investigated. Upon *S. aureus* infection, the rats' blood inflammation indicators of lymphocytes (LY), white blood cells (WBC) and

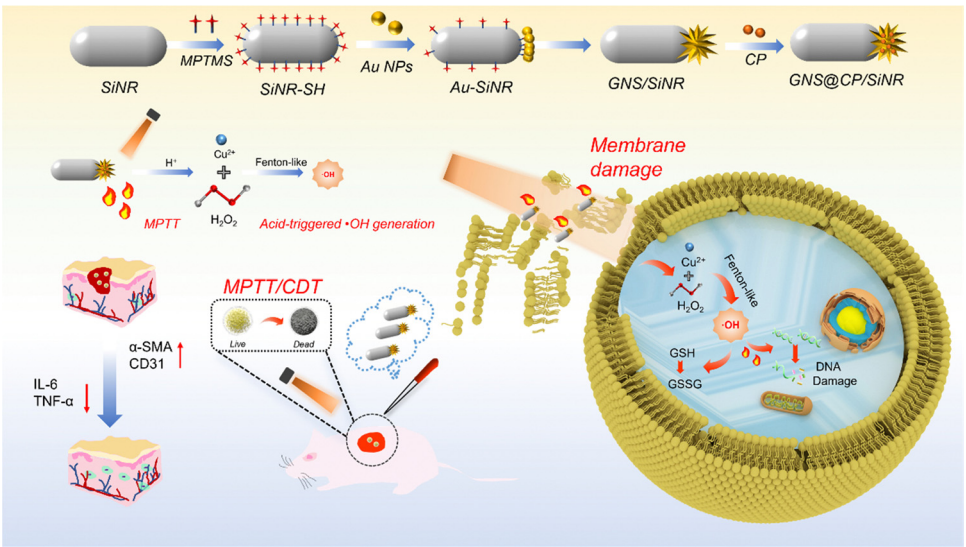

Scheme 1 Illustration of the synthetic route of the GNS@CP/SiNR Janus nanostructure, its NIR II mild photothermal effect and acid-triggered •OH generation properties, and the synergistic MPTT/CDT antibacterial application and mechanism.

Published on 18 kwietnia 2024. Downloaded on 21.04.2026 23:01:02.

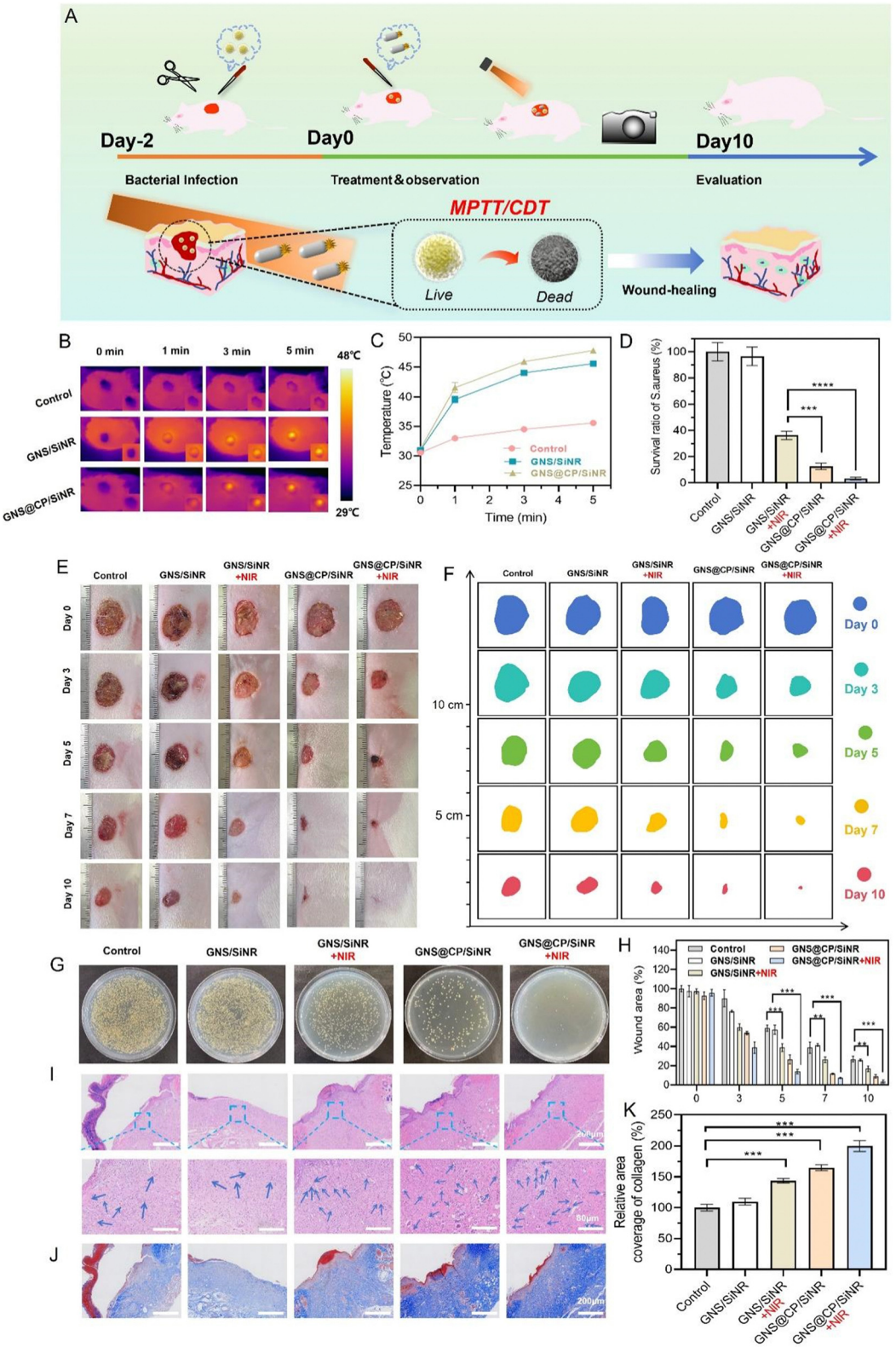

Fig. 7 *In vivo* synergistic MPTT/CDT antibacterial and wound healing effect of GNS@CP/SiNR. (A) Scheme shows the *in vivo* experimental protocols. (B) Thermal images showing the *in vivo* photothermal effect of GNS@CP and GNS@CP/SiNR, and the corresponding time-temperature curves (C). (D) Survival rate of *S. aureus* in rats' wounds after 10 days with different treatments. (E) Digital images showing the wound closure process along with time in different treated groups. (F) Images show the rat's wound shape with different treatments in different days, which was drawn by Adobe Illustrator software. (G) Agar plates showing the remanent bacterial colonies in different treated groups after 10 days treatment. (H) Histogram showing the wound healing efficiency of different treatments along with time. H&E (I) and Masson (J)-stained histological images of wounds after 10 days different treatments, and the corresponding histogram showing the coverage of collagen in the rat's wound (K). Blue arrows indicate the number of vessels in the skin tissues.

 This journal is © The Royal Society of Chemistry 2024

Published on 18 kwietnia 2024. Downloaded on 21.04.2026 23:01:02.

neutrophils (NEUT) increased abnormally (Fig. 8A–C). The GNS/SiNR+NIR and GNS@CP/SiNR treatments could largely reduce the levels of the above three blood indicators, while the GNS@CP/SiNR+NIR treatment decreased those three blood indicators to the normal values seen in healthy rats. Pro-inflammatory cytokines of IL-6 and TNF-α in skin wound tissues were also examined by immunohistochemical analysis (Fig. 8D–F). Similarly, the GNS@CP/SiNR+NIR treatment significantly decreased the expression levels of both IL-6 and TNF-α *via* the synergistic MPTT/CDT anti-inflammation effect. Improvement in the inflammation microenvironment can promote skin wound tissue regeneration, where angiogenesis is an important step during the wound-healing process.[35] Because α-smooth muscle actin (α-SMA) and platelet endothelial cell adhesion molecule (CD31) are important indicators of angiogenesis,[36] the α-SMA and CD31 double immunofluorescence staining assay was performed to evaluate the new blood vessel formation in different treated groups (Fig. 8G and H). In the control groups, only limited green and red fluorescent spots could be visualized, indicating that few new blood vessels were formed in the wound tissues. Expression levels of α-SMA and CD31 in the GNS/SiNR+NIR and GNS@CP/SiNR-treated groups clearly increased, suggesting that the MPTT or CDT effect could promote angiogenesis to accelerate wound healing.

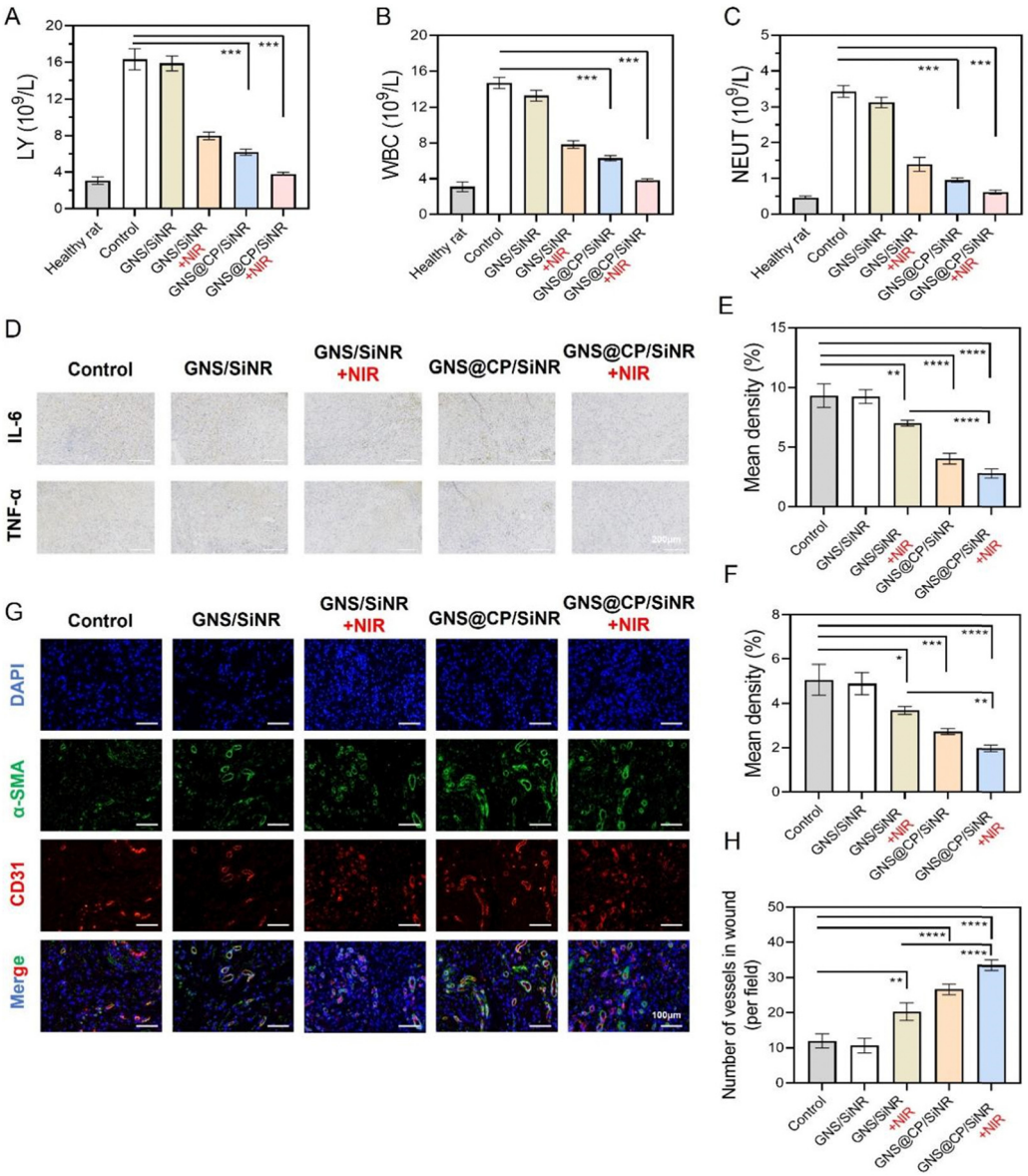

Fig. 8 *In vivo* wound healing mechanism of GNS@CP/SiNR. Blood chemistry parameters of (A) lymphocyte (LY), (B) white blood cell (WBC) and (C) neutrophil (NEUT) counts after 10 days different treatments. (D) Immunohistochemical images of IL-6 and TNF-α in the rats' wound tissues after 10 days different treatments, and the corresponding semi-quantitative expression levels of IL-6 (E) and TNF-α (F). Scale bar represents 200 μm. (G) Immunofluorescent CD31/α-SMA stained images of the rats' wound tissues after 10 days different treatments, and the semi-quantitative analysis on the number of blood vessels in the wounds (H). Scale bar represents 100 μm.

Published on 18 kwietnia 2024. Downloaded on 21.04.2026 23:01:02.

Significantly, the GNS@CP/SiNR+NIR treatment resulted in the highest expression level of both α-SMA and CD31, indicating that MPTT and CDT could synergistically induce angiogenesis to promote wound-healing.

3.7 Biocompatibility evaluation of GNS@CP/SiNR

To evaluate the biocompatibility of GNS@CP/SiNR, the cell compatibility of GNS@CP/SiNR with varied concentrations was examined on mouse embryonic fibroblasts (NIH/3T3) using the CCK-8 assay. It showed that that the cell viability was reduced to some extent by increasing the concentration of GNS@CP/SiNR. However, the cell viability was still higher than 80% when the concentration of the materials reached 200 μg mL^{-1}, indicating the good cytocompatibility of GNS@CP/SiNR (Fig. S19, ESI†). To investigate the *in vivo* biocompatibility of GNS@CP/SiNR, H&E staining assay on the rats' major organs (heart, liver, spleen, lungs, kidneys) and blood routine biochemical analysis were performed after different treatments. H&E images showed that no obvious damage could be observed in the rats' main organs (Fig. S20, ESI†), and the blood routine biochemical analysis results showed that all blood indicators were maintained within the normal range of healthy rats (Fig. S21, ESI†). Additionally, the body weight of rats in different treatment groups remained at a relatively stable range during the whole treatment period (Fig. S22, ESI†). All of these results demonstrated the excellent histocompatibility and blood compatibility of GNS@CP/SiNR and the related treatments, which guarantees the safe use of GNS@CP/SiNR for biomedical applications.

4. Conclusion

In the present work, a multifunctional GNS@CP/SiNR Janus nanostructure was designed and fabricated. Due to the particular Janus nanostructure and CP nanodots decoration, GNS@CP/SiNR displayed both NIR-II laser-induced mild photothermal effect and self-activated $^{\bullet}OH$ generation ability, which enabled the nanosystem to perform synergistic MPTT/CDT applications. Both *in vitro* and *in vivo* evaluations demonstrated that GNS@CP/SiNR was effective for antibacterial, anti-biofilm and wound healing applications. Our mechanism study elucidated that GNS@CP/SiNR inhibited bacterial growth by ways of causing bacterial membrane damage, boosting the intracellular ROS, depleting the intracellular GSH and triggering DNA damage. The findings of our work provide a promising material for the highly-efficient treatment of wound infections.

Author contributions

Y. L., R. X. and W. L. contributed equally to this work. S. Y. designed the work, analyzed the data and wrote the manuscript. Y. L., R. X. and W. L. performed the experiments, collected and analyzed the data. W. C. and Y. F. helped in some experiments, W. X. and S. Y. provided the funding. All authors have given approval to the final version of the manuscript.

Conflicts of interest

There are no conflicts to declare.

Acknowledgements

S. Y. acknowledges the Guangzhou Science and Technology Planning Project (2023A03J0059), Guangdong Basic and Applied Basic Research Foundation (2021A1515011063), and the Fundamental Research Funds for the Central Universities (21622107). W. X. acknowledges the Guangdong Basic and Applied Basic Research Foundation (2022A1515012148), and the Science and Technology Program of Guangzhou (202103030003 and 202103030004).

References

1 K. S. Ikuta, L. R. Swetschinski, G. R. Aguilar, F. Sharara, T. Mestrovic, A. P. Gray, N. D. Weaver, E. E. Wool, C. Han and A. G. Hayoon, Global mortality associated with 33 bacterial pathogens in 2019: a systematic analysis for the Global Burden of Disease Study 2019, *The Lancet*, 2022, **400**(10369), 2221–2248.
2 X. Zhen, C. S. Lundborg, X. Sun, X. Hu and H. Dong, Economic burden of antibiotic resistance in ESKAPE organisms: a systematic review, *Antimicrobial Resistance & Infection Control*, 2019, **8**, 1–23.
3 G. Dhanda, P. Sarkar, S. Samaddar and J. Haldar, Battle against vancomycin-resistant bacteria: recent developments in chemical strategies, *J. Med. Chem.*, 2018, **62**(7), 3184–3205.
4 R. P. Willems, K. van Dijk, M. J. Vehreschild, L. M. Biehl, J. C. Ket, S. Remmelzwaal and C. M. Vandenbroucke-Grauls, Incidence of infection with multidrug-resistant Gram-negative bacteria and vancomycin-resistant enterococci in carriers: a systematic review and meta-regression analysis, *Lancet Infect. Dis.*, 2023, **23**(6), 719–731.
5 X. Qi, Y. Xiang, E. Cai, X. Ge, X. Chen, W. Zhang, Z. Li and J. Shen, Inorganic–organic hybrid nanomaterials for photothermal antibacterial therapy, *Coord. Chem. Rev.*, 2023, **496**, 215426.
6 W. He, D. Lv, Y. Guan and S. Yu, Post-synthesis modification of metal–organic frameworks: synthesis, characteristics, and applications, *J. Mater. Chem. A*, 2023, **11**(45), 24519–24550.
7 J. Huo, Q. Jia, H. Huang, J. Zhang, P. Li, X. Dong and W. Huang, Emerging photothermal-derived multimodal synergistic therapy in combating bacterial infections, *Chem. Soc. Rev.*, 2021, **50**(15), 8762–8789.
8 D. Zhi, T. Yang, J. O'hagan, S. Zhang and R. F. Donnelly, Photothermal therapy, *J. Controlled Release*, 2020, **325**, 52–71.
9 S. Yu, G. Huang, R. Yuan, T. Chen and A. uPAR, targeted nanoplatform with an NIR laser-responsive drug release property for tri-modal imaging and synergistic photothermal-chemotherapy of triple-negative breast cancer, *Biomater. Sci.*, 2020, **8**(2), 720–738.
10 B. Li, Q. Zhou, H. Wang, Y. Zha, P. Zheng, T. Yang, D. Ma, L. Qiu, X. Xu and Y. Hu, Mitochondria-targeted magnetic gold nanoheterostructure for multi-modal imaging guided photothermal and photodynamic therapy of triple-negative breast cancer, *Chem. Eng. J.*, 2021, **403**, 126364.

 This journal is © The Royal Society of Chemistry 2024

Published on 18 kwietnia 2024. Downloaded on 21.04.2026 23:01:02.

11 Z. Liang, W. Liu, Z. Wang, P. Zheng, W. Liu, J. Zhao, Y. Zhong, Y. Zhang, J. Lin and W. Xue, Near-infrared laser-controlled nitric oxide-releasing gold nanostar/hollow polydopamine Janus nanoparticles for synergistic elimination of methicillin-resistant Staphylococcus aureus and wound healing, *Acta Biomater.*, 2022, **143**, 428–444.
12 N. Fernandes, C. F. Rodrigues, A. F. Moreira and I. J. Correia, Overview of the application of inorganic nanomaterials in cancer photothermal therapy, *Biomater. Sci.*, 2020, **8**(11), 2990–3020.
13 S. Liu, X. Pan and H. Liu, Two-dimensional nanomaterials for photothermal therapy, *Angew. Chem.*, 2020, **132**(15), 5943–5953.
14 L. Shi, L. A. Sordillo, A. Rodríguez-Contreras and R. Alfano, Transmission in near-infrared optical windows for deep brain imaging, *J. Biophotonics*, 2016, **9**(1–2), 38–43.
15 C. Li, G. Chen, Y. Zhang, F. Wu and Q. Wang, Advanced fluorescence imaging technology in the near-infrared-II window for biomedical applications, *J. Am. Chem. Soc.*, 2020, **142**(35), 14789–14804.
16 Q. Zhu, W. Jiang, K. Ye, S. Jin, W. Dong, S. Liu, G. Zhang, C. Tian, Y. Luo and Y. Wang, Hydrogenated Oxide Material for Self-Targeting and Automatic-Degrading Photothermal Tumor Therapy in the NIR-II Bio-Window, *Adv. Funct. Mater.*, 2022, **32**(14), 2110881.
17 Z.-H. Wu, M. Peng, C. Ji, P. Kardasis, I. Tzourtzouklis, M. Baumgarten, H. Wu, T. Basché, G. Floudas, M. Yin and A. Terrylene–Anthraquinone Dyad, as a Chromophore for Photothermal Therapy in the NIR-II Window, *J. Am. Chem. Soc.*, 2023, **145**(48), 26487–26493.
18 S. Guo, D. Tang, M. Zhang, H. Yang, T. Zhang, B. Hu, C. Xu, Y. Weng, K. Shang and Y. Huang, Spatiotemporal-Controlled NIR-II Immune Agonist Sensitizes Cancer Immunotherapy, *Adv. Mater.*, 2024, 2400228.
19 W. Liu, X. Song, W. Liu, Q. Lin, R. Xu, H. Li, W. Xue and S. Yu, Mild-Temperature Photothermal Effect Triggers Simultaneous Nitric Oxide-and Deferoxamine-Releasing Mesoporous Polydopamine-Based Nanoplatform for Robust Antibacterial, Anti-inflammation, and Wound-Healing Activity, *Chem. Mater.*, 2022, **34**(23), 10606–10622.
20 G. Gao, Y. W. Jiang, Y. Guo, H. R. Jia, X. Cheng, Y. Deng, X. W. Yu, Y. X. Zhu, H. Y. Guo and W. Sun, Enzyme-mediated tumor starvation and phototherapy enhance mild-temperature photothermal therapy, *Adv. Funct. Mater.*, 2020, **30**(16), 1909391.
21 S. Dong, Y. Dong, Z. Zhao, J. Liu, S. Liu, L. Feng, F. He, S. Gai, Y. Xie and P. Yang, ''Electron Transport Chain Interference'' Strategy of Amplified Mild-Photothermal Therapy and Defect-Engineered Multi-Enzymatic Activities for Synergistic Tumor-Personalized Suppression, *J. Am. Chem. Soc.*, 2023, **145**(17), 9488–9507.
22 X. Meng, Z. Sun, H. Chu and Y. Wang, Self-assembled nanoplatforms for chemodynamic therapy, *Chem. Eng. J.*, 2023, 147702.
23 H. Lin, Y. Chen and J. Shi, Nanoparticle-triggered in situ catalytic chemical reactions for tumour-specific therapy, *Chem. Soc. Rev.*, 2018, **47**(6), 1938–1958.
24 C. Jia and F.-G. Wu, Antibacterial Chemodynamic Therapy: Materials and Strategies, *BME Front.*, 2023, **4**, 0021.
25 Y. Shen, C. Nie, T. Pan, W. Zhang, H. Yang, Y. Ye and X. Wang, A multifunctional cascade nanoreactor based on Fe-driven carbon nanozymes for synergistic photothermal/chemodynamic antibacterial therapy, *Acta Biomater.*, 2023, **168**, 580–592.
26 Q. Zhang, J. Wu, J. Wang, X. Wang, C. Wu, M. Chen, Q. Wu, M. S. Lesniak, Y. Mi and Y. Cheng, A neutrophil-inspired supramolecular nanogel for magnetocaloric–enzymatic tandem therapy, *Angew. Chem.*, 2020, **132**(9), 3761–3767.
27 X. Fang, S. Cai, M. Wang, Z. Chen, C. Lu and H. Yang, Photogenerated holes mediated nitric oxide production for hypoxic tumor treatment, *Angew. Chem., Int. Ed.*, 2021, **60**(13), 7046–7050.
28 J. He, L.-H. Fu, C. Qi, J. Lin and P. Huang, Metal peroxides for cancer treatment, *Bioact. Mater.*, 2021, **6**(9), 2698–2710.
29 W. Wu, Y. Yang, Y. Zhang, Y. Zeng, Z. Liang, X. Song, Y. Huang, W. Xue and S. Yu, Biodegradable copper peroxide decorated hollow polydopamine nanocomposite as effective chloroperoxidase delivery carrier for enhancing enzyme dynamic therapy via self-activated cascade reactions, *Chem. Eng. J.*, 2024, **481**, 148113.
30 L.-S. Wang, A. Gupta and V. M. Rotello, Nanomaterials for the treatment of bacterial biofilms, *ACS Infect. Dis.*, 2016, **2**(1), 3–4.
31 S. Yu, G. Li, R. Liu, D. Ma and W. Xue, Dendritic Fe_3O_4@ poly (dopamine)@ PAMAM nanocomposite as controllable NO-releasing material: a synergistic photothermal and NO antibacterial study, *Adv. Funct. Mater.*, 2018, **28**(20), 1707440.
32 H. Li, X. Song, W. Liu, Y. Zhang, H. Guan, J. Wu, S. Yu and W. Xue, Revealing the antibacterial power of hydrogen-releasing PdH nanohydride against drug resistant Staphylococcus aureus: an in-depth mechanism study, *J. Mater. Chem. B*, 2023, **11**(7), 1495–1505.
33 J. Li, W. Yi, Y. Luo, K. Yang, L. He, C. Xu, L. Deng and D. He, GSH-depleting and H_2O_2-self-supplying hybrid nanozymes for intensive catalytic antibacterial therapy by photothermal-augmented co-catalysis, *Acta Biomater.*, 2023, **155**, 588–600.
34 S. Yu, G. Li, P. Zhao, Q. Cheng, Q. He, D. Ma and W. Xue, NIR-laser-controlled hydrogen-releasing PdH nanohydride for synergistic hydrogen-photothermal antibacterial and wound-healing therapies, *Adv. Funct. Mater.*, 2019, **29**(50), 1905697.
35 S. A. Eming, B. Brachvogel, T. Odorisio and M. Koch, Regulation of angiogenesis: wound healing as a model, *Progress Histochem. Cytochem.*, 2007, **42**(3), 115–170.
36 Y. Zhang, P. Zhang, X. Gao, L. Chang, Z. Chen and X. Mei, Preparation of exosomes encapsulated nanohydrogel for accelerating wound healing of diabetic rats by promoting angiogenesis, *Mater. Sci. Eng., C*, 2021, **120**, 111671.